



# Two-Dimensional MXene as a Nanofluidic Anolyte Additive for Enhancing Performance of Vanadium Redox Flow Batteries

Ali Vala Mizrak,<sup>[a]</sup> Jonathan C. Ehring,<sup>[a]</sup> Mikhail Shekhirev,<sup>[b]</sup> Robert W. Lord,<sup>[b]</sup> Bilen Aküzüm,<sup>[b, c]</sup> Pushpendra Singh,<sup>[b]</sup> Yury Gogotsi,<sup>[b]</sup> and E. Caglan Kumbur<sup>\*[a]</sup>

In this work,  $Ti_3C_2T_x$  MXene was investigated as a nanofluidic anolyte additive in vanadium redox flow batteries to improve the sluggish kinetics of  $V^{2+}/V^{3+}$  redox reaction. Numerous electrochemical tests under flow and static conditions were performed to demonstrate the effectiveness of MXenes for VRFB applications. Pressure drop tests and morphology analysis were also conducted to better understand the hydraulic effects of MXene addition into the anolyte. The nanofluidic anolytes with the concentration of 0.10 and 0.15 wt% showed the best electrochemical performance, although the former induced less aggravated hydraulic effects within a reasonable pressure drop range. At a current density of  $200 \text{ mA cm}^{-2}$ , the nanofluidic

analyte containing 0.10 wt% MXene was able to utilize 67% of the theoretical capacity. Contrarily, with the pristine anolyte, only 10% of the theoretical capacity could be utilized due to excessive losses. Moreover, the energy efficiency up to 74% is observed for the nanofluidic electrolyte, which is an increase of 25% compared to the pristine anolyte. Primarily, the enhanced battery performance was attributed to the improved electrocatalytic activity towards the anodic  $V^{2+}/V^{3+}$  redox reaction. Furthermore, a dynamic, web-like, flowing electrode network is shown to increase the mass transport capacity of porous carbon felt electrodes by creating additional, abundant, and electrochemically active surfaces within the pores.

## Introduction

The global energy industry is increasingly shifting focus towards the utilization of the renewable energy resources (e.g., wind, geothermal and solar power) to address emerging environmental concerns. Consequently, clean energy is becoming a global trend in many industrialized countries to reduce greenhouse gas emissions.<sup>[1]</sup> Nonetheless, electricity generation from renewable resources requires intermediary storage technologies since the fluctuant and intermittent nature of these resources may cause grid destabilizations, and power interruptions. Ruminating these factors, reliable, safe, and flexible grid-scale energy storage systems are imperative to rely predominantly on renewables.<sup>[2]</sup> Redox flow batteries being a well-

established, inherently safe, highly modular, and adaptable energy storage technology, can offer a solution to bridge the gap between the adaptation of renewable resources and the recent demands of the energy market.<sup>[3]</sup> Among several chemistries, vanadium redox flow batteries (VRFBs) have been studied more intensely due to their compelling advantages such as manageability of cross-contamination, safety, and long service life.<sup>[4]</sup>

Since Skyllas-Kazacos et al. had first proposed the VRFB almost three decades ago,<sup>[5]</sup> numerous investigations have advanced the feasibility of this system.<sup>[6]</sup> Yet, there are still challenges that hinder the widespread commercial availability. The high price of the vanadium metal and expensive battery components together with the comparatively low energy density of this electrochemical system are the primary drawbacks that impede the utilization of VRFBs on a larger scale. Projections for 2025 indicates that the price will be around 400 \$/kWh for VRFB technology, which is higher than Li-ion batteries.<sup>[7]</sup> To date, efforts to improve the efficiencies and electrochemical performance of the VRFBs have been concentrated on lowering the internal overpotentials that are caused by the kinetic activation, ohmic, and mass transport losses.<sup>[6,8–11]</sup> Studies on the system design along with modelling and simulation to enhance the operational capability of VRFBs,<sup>[12–14]</sup> as well as studies focusing on high-energy density electrolyte development with improved solubility of active species have been reported.<sup>[15,16]</sup> The stability of the electrolytes was exclusively studied at different environmental conditions,<sup>[17]</sup> and in that respect, numerous additives were investigated to prevent precipitation of the reacting metal salts (i.e., vanadium sulfate) by extending the operating temperature range.<sup>[18]</sup>

[a] A. Vala Mizrak, J. C. Ehring, Prof. Dr. E. C. Kumbur  
Electrochemical Energy Systems Laboratory  
Department of Mechanical Engineering and Mechanics  
Drexel University  
Philadelphia, PA 19104 USA  
E-mail: eck32@drexel.edu

[b] Dr. M. Shekhirev, Dr. R. W. Lord, Dr. B. Aküzüm, Dr. P. Singh,  
Prof. Dr. Y. Gogotsi  
A. J. Drexel Nanomaterials Institute & Department of Materials Science and  
Engineering  
Drexel University  
Philadelphia, PA 19104 USA

[c] Dr. B. Aküzüm  
Energy Storage and Distributed Resources Division  
Lawrence Berkeley National Laboratory  
Berkeley, California 94720, United States

Supporting information for this article is available on the WWW under  
<https://doi.org/10.1002/batt.202200321>

An invited contribution to a Special Collection dedicated to the 5-Year Anniversary of Batteries & Supercaps

Besides these, addition of nanoparticles into electrolytes have also been investigated as a medium to indirectly boost electrochemical performance of VRFBs. Despite nanofluids being a well-known phenomenon with plentiful applications in various areas (i.e., heat transfer, tribological, pharmaceutical/medical, and environmental applications etc.),<sup>[19–21]</sup> there have been only a handful of studies that have adapted this concept into flow battery research.

Nanofluidic electrolytes in flow batteries were not utilized initially in all-vanadium systems. Duduta et al. demonstrated a prototype for a semi-solid flow cell system using flowing lithium-ion cathode and anode suspensions, and they reported greater energy density values compared to the regular flow batteries as well as higher cell voltages due to the non-aqueous suspensions.<sup>[22]</sup> Considering the adaptation of the concept of nanofluidic electrolytes into the field of VRFBs, limited research has been conducted so far. Hatzell et al. employed activated carbon spheres and multi-walled carbon nanotubes (MWCNTs) as conducting particles in a flow battery electrolyte containing the  $\text{VO}^{2+}/\text{VO}_2^+$  redox couple for the first time,<sup>[23]</sup> and demonstrated that the particles facilitated both faradaic and electric double layer charge storage. The study was only limited to testing under a two-electrode static configuration. With a gravimetric ratio of 1:10 (solid:liquid), utilizing MWCNT containing flow-electrodes in a VRFB catholyte, they reported 10 times more energy, and 20 times greater power densities. Lobato et al. employed graphene nanoplatelets powder in an all-vanadium battery system,<sup>[24]</sup> and the nanofluidic electrolytes were tested in realistic conditions based on the recordings of the solar radiation at a certain location in Spain. It was shown that the utilization of nanofluidic electrolytes promoted higher voltaic efficiencies, and the charge capacity increased more than 14%. Furthermore, a lower capacity fade was observed. In the same year, Aaron et al. utilized Vulcan XC-72R, and rGO as nanoparticle additives but focused on the deposition of particles onto the electrode rather than as a nanofluidic electrolyte approach. By utilizing carbon felt electrodes to avoid clogging, current density values associated with the voltaic efficiency of 80% increased from  $53.1 \text{ mA cm}^{-2}$  to 133, and  $161 \text{ mA cm}^{-2}$  for rGO and Vulcan XC-72R particles, respectively. These results indicated a trade-off between kinetic improvement and the inhibiting effect of aggravated mass transport overpotentials because of the presence of carbon particles. However, a more systematical approach is needed to better understand the effects of particles concentration and preparation method on kinetic performance. Later, multi-walled carbon nanotubes (MWCNTs) have been investigated by Kim et al. for VRFBs,<sup>[25]</sup> and various ratios of the nanoparticles for nanofluidic electrolytes were tested to understand the effect of additive concentration to the electrochemical performance. Compared to the pristine electrolytes, higher capacity utilization was shown along with the improved reaction kinetics for the  $\text{V}^{+2}/\text{V}^{+3}$  and  $\text{VO}^{2+}/\text{VO}_2^+$  redox couples. They also proposed a hybrid electrode, comprising a carbon foam electrode sandwiched between two carbon felts.<sup>[26]</sup> Together with the novel hybrid electrodes, nanofluidic electrolytes showed a decrease in pumping loads, and the battery performance improved with

the discharge capacity and the capacity retention increased by 16.8%, and 5.2 times, respectively. Additionally, Kim et al. investigated nanofluidic electrolytes containing MWCNT and MWCNT-COOH nanoparticles.<sup>[27]</sup> The particles were added to the electrolytes with a concentration of 0.1 wt%, and 4.2 mm thick carbon felts were utilized as electrodes. They reported that the activation overpotentials decreased at a relatively high current density of  $120 \text{ mA cm}^{-2}$ , and a higher battery performance was achieved, but the enhanced mass transport properties played a more significant role. More interestingly, the catholyte was found to be less responsive to the change of the surface group of the nano additive, while the nanofluidic anolyte performance was strongly dependent on the presence of carboxylic functional groups (i.e.,  $-\text{COOH}$ ).

In the same year, GO particles with a degree of oxidation of about 22% were investigated by Aberoumand et al. as a nanofluidic electrolyte additive.<sup>[28]</sup> Even though no electrochemical data was reported in that study, rheological behavior, electrical/thermal conductivity, and colloidal stability were investigated with respect to varying weight fractions of GO particles. Regarding these methods, the nanofluidic electrolyte containing GO particles with a concentration of 0.05 wt% was found to be showing optimal properties. More recently, the same group reported more on the electrochemical performance of rGO flakes as a nanofluidic additive.<sup>[29]</sup> The nanofluidic electrolytes containing rGO particles with concentrations of 0.1 to 0.6 wt% were prepared and electrochemical data was supported with examination of the morphological characteristics along with the colloidal stability and viscosity measurements. Based on cyclic voltammetry, for the best performing nanofluidic electrolyte with an additive load of 0.4 wt%, the peak potential separation, and limiting current density rates were reported to increase by 15 and 20 times, respectively. However, the electrochemical performance of the nanofluidic additives in this study was investigated only with a static, three-electrode cell. Therefore, to reveal the actual performance of these particles in an operating flow cell, flow battery tests are still required.

It is noteworthy that all these studies have primarily investigated carbonaceous particles, which are hydrophobic in nature and may require additional treatments (e.g., oxidation, attaching functional groups, etc.) to increase their dispersibility in aqueous environments. On the contrary, hydrophilicity is one of the most crucial properties that defines the suitability of a nanoparticle to be utilized as a nanofluidic additive under flowing conditions. Delaminated, two-dimensional titanium carbide ( $\text{Ti}_3\text{C}_2\text{T}_x$ ) MXene has shown favorable hydrophilicity due to abundant surface groups (i.e.,  $-\text{OH}$ ,  $-\text{O}$ , and  $-\text{F}$ ; represented by  $\text{T}_x$ ) which are formed during the synthesis process. Moreover, MXene is also highly stable in low pH environments and exceptionally conductive (up to  $20,000 \text{ S cm}^{-1}$ ).<sup>[30]</sup> Another advantageous feature that  $\text{Ti}_3\text{C}_2\text{T}_x$  MXene offers is the formation of 3D structures from agglomerated 2D  $\text{Ti}_3\text{C}_2\text{T}_x$  flakes in low-pH solutions known as *crumbling*.<sup>[31]</sup> This effect can increase the electrochemically active surface area due to the porous and open architecture of the crumbled particles and thus the kinetics of the anodic  $\text{V}^{+2}/\text{V}^{+3}$  redox reactions can be

facilitated. On the other hand, MXene have already found applications in various areas such as energy storage, catalysis, medicine, and electronics.<sup>[32–41]</sup> Furthermore, we have recently shown the catalytic activity of  $Ti_3C_2T_x$  flakes for the anodic  $V^{+2}/V^{+3}$  redox reactions by proposing a simple drop casting procedure to modify carbon paper electrodes with delaminated  $Ti_3C_2T_x$  nanoflakes in VRFBs.<sup>[42]</sup> MXene coating on negative electrodes resulted in higher battery efficiencies and enhanced electrolyte utilization rates, which remarkably improved the battery performance.

In this work, delaminated  $Ti_3C_2T_x$  MXene has been investigated as a nano-additive in VRFB anolyte which provides a stable chemical environment for  $Ti_3C_2T_x$  flakes since they quickly degrade under positive potentials.<sup>[34]</sup> Nanofluidic anolytes containing four different weight percentages of MXene flakes (0, 0.05, 0.10, and 0.15 wt%) were studied in terms of their catalytic performance towards the  $V^{+2}/V^{+3}$  redox couple, and a facile method for the preparation of MXene based nanofluidic anolytes was described. In that respect, flow battery testing such as polarization curves, load curves, electrochemical impedance spectroscopy (EIS), and charge-discharge cycle analyses along with the pressure drop measurements were conducted to thoroughly investigate the effect of utilization of the nanofluidic anolytes to the overall battery performance. Furthermore, material characterization techniques were employed to assess the battery performance data in depth. X-ray diffraction (XRD), transmission electron microscopy (TEM),

selected area electron diffraction (SAED), and atomic force microscopy (AFM) were used to characterize MXene flakes, while optical microscopy was performed to visualize particle distribution, at varying MXene concentration. In addition, scanning electron microscopy (SEM) was used to understand MXene-electrode interactions and their morphological changes.

## Results and Discussion

### Characterization of MXene and the nanofluidic anolytes

The synthesis of MXene flakes was performed following the previously published protocol<sup>[43]</sup> by selective etching of Al from  $Ti_3AlC_2$  precursor and delaminating the resultant multilayer particles with LiCl solution. XRD was performed to show the complete etching of the Al layers from  $Ti_3AlC_2$  and formation of  $Ti_3C_2T_x$  structures (Figure S1). The expansion and disorder of the interlayer spacing, which can be observed by the shift and widening of the (002) peak, indicates a successful exfoliation process of MXene nanoflakes. Furthermore, the complete transformation of MAX phase into the MXene flakes can be seen by the fact that (014) peak vanished and only (00l) series of peaks is present in the XRD of the  $Ti_3C_2T_x$  film.

The successful fabrication of solution of single-layer MXene was further confirmed by TEM and AFM analysis. Figure 1(a) shows a TEM image of a MXene flake. SAED image of the single

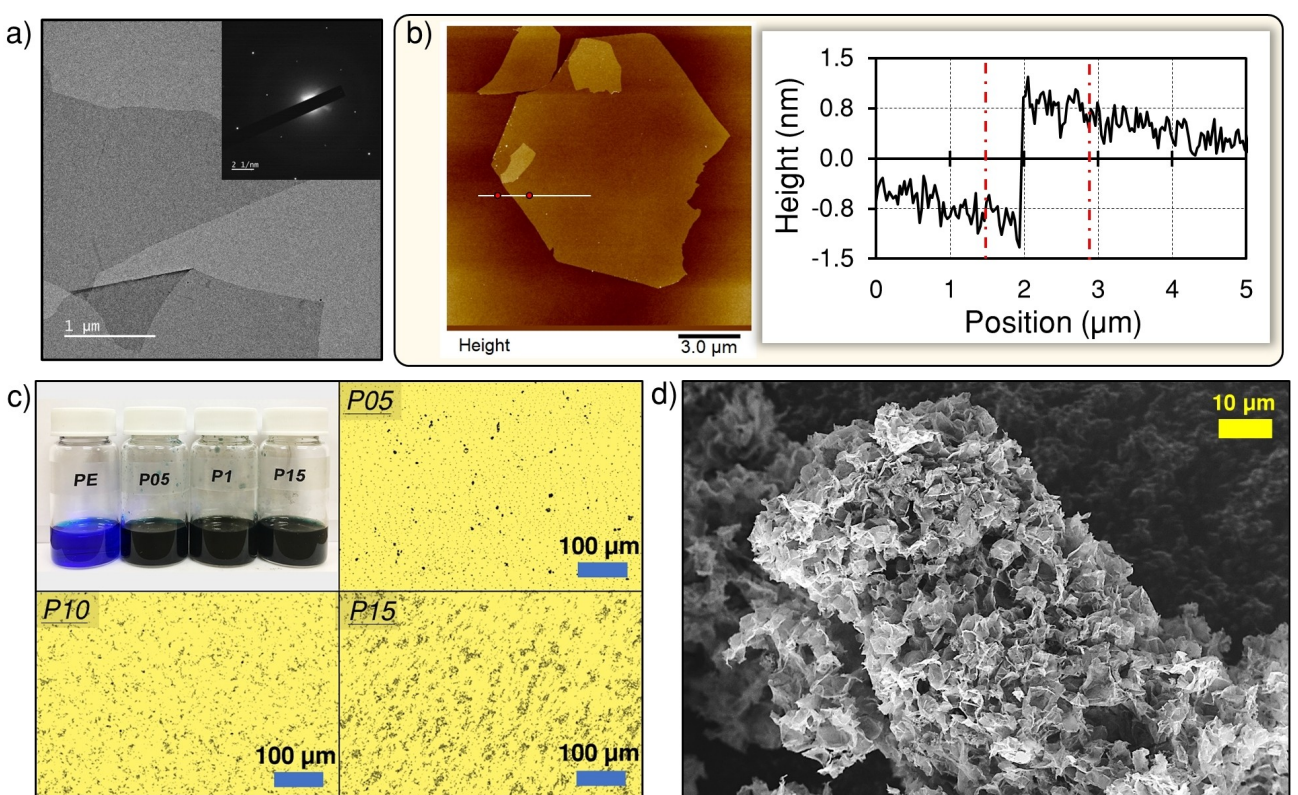


**Figure 1.** a) TEM image of a MXene flake and SAED pattern; b) AFM image and height profile; c) photo of the vials with the anolytes containing different concentration of MXene additive and optical microscopy images of the nanofluidic electrolytes deposited on glass substrate; d) SEM image of crumbled MXene flakes.

flake shows hexagonal symmetry, demonstrating that the symmetry of the basal plane of the MAX precursor is preserved after HF etching. Figure 1(b) shows a typical AFM image of several flakes deposited on Si/SiO<sub>2</sub> substrate. The step height at the edge of one of the flakes measures at approximately 2 nm, corresponding to single-layer MXene flake. This thickness is larger than the theoretically predicted thickness of a monolayer Ti<sub>3</sub>C<sub>2</sub>T<sub>x</sub> nano flake due to water molecules present in between the flake and the substrate and is consistent with the previously measured single-layer sheets.<sup>[44]</sup> Furthermore, microscopic analysis indicates the polydisperse nature of the sample, where the size of the flakes varies and goes up to 10 μm in lateral size. Based on the DLS results, the average flake size of the MXene nanoflakes in the final suspension was found to be 1.7 μm.<sup>[45]</sup>

The particle distribution in the nanofluidic anolytes can be seen in Figure 1(c). An image capturing each nanofluidic anolyte in vials, along with the PE anolyte, is also shown in the same figure at the top-left corner. The image indicates that, with the addition of Ti<sub>3</sub>C<sub>2</sub>T<sub>x</sub> nanoparticles to the base anolyte (PE), the color of the electrolyte turned an opaque dark-blue from a lighter translucent blue color. The nanofluidic anolytes were also monitored for 6 months to investigate the stability of the suspensions. MXene sedimentation has not been observed, indicating a very good suspension stability. Microscope images showed that the average agglomeration size of the MXene nanoflakes increases with concentration of the particles. While the P05 anolyte showed a distribution of exceedingly small and point-like particles together with some rare and larger blocks of MXenes, the P10 anolyte had much larger aggregates that exhibited varying sizes. In the P15 anolyte with the highest MXene concentration, the aggregates of Ti<sub>3</sub>C<sub>2</sub>T<sub>x</sub> formed even larger agglomerates and clusters creating a continuous particle web. Furthermore, the size of the clusters became more

distinguishable to the eye. Based on the optical microscopy images, the cluster sizes can reach up to 50 μm in length.

In addition to the microscopic investigation of the size and distribution of Ti<sub>3</sub>C<sub>2</sub>T<sub>x</sub> flakes in the anolytes, the crumpling effect on 2D MXene flakes was also studied by SEM (Figure 1d). The SEM image reveals that foam-like 3D structures were established after treatment of MXene flakes with the PE electrolyte. Because of the crumpling effect, 2D MXene would flocculate into porous crumpled flakes in such low pH solutions. Therefore, in a VRFB system, MXene added to anolyte would be highly prone to crumpling due to the acidic nature of the electrolyte containing 4 M sulfuric acid. Consequently, large electrochemically active surface area of flocculated porous 3D MXene particles with an open architecture enhanced the kinetics of anodic V<sup>2+</sup>/V<sup>3+</sup> redox reaction.

The SEM images for morphological characteristics of the pristine carbon felt electrodes and those which interacted with MXene are presented in Figure 2. The plain carbon felt electrode exhibited a regular morphological structure. The diameter of a single fiber in carbon felt electrodes was observed to be about 20 μm. Since the carbon fibers are randomly and densely distributed, the electrodes demonstrate an irregular configuration of fibers with varying sizes of pores, slots, and tunnels throughout their porous structure. Therefore, utilization of nanofluidic anolytes containing dense flocs of nanoparticles may lead to higher pressure drops in flow batteries, which was also investigated in the context of this study.

In Figure 2(b and c), neither a binder material nor any significant amount of residual electrolyte was observed on the fibers of the felt that was used with the pristine anolyte. The individual fibers had a grooved surface formation that extended along the length of the fibers. The images indicate

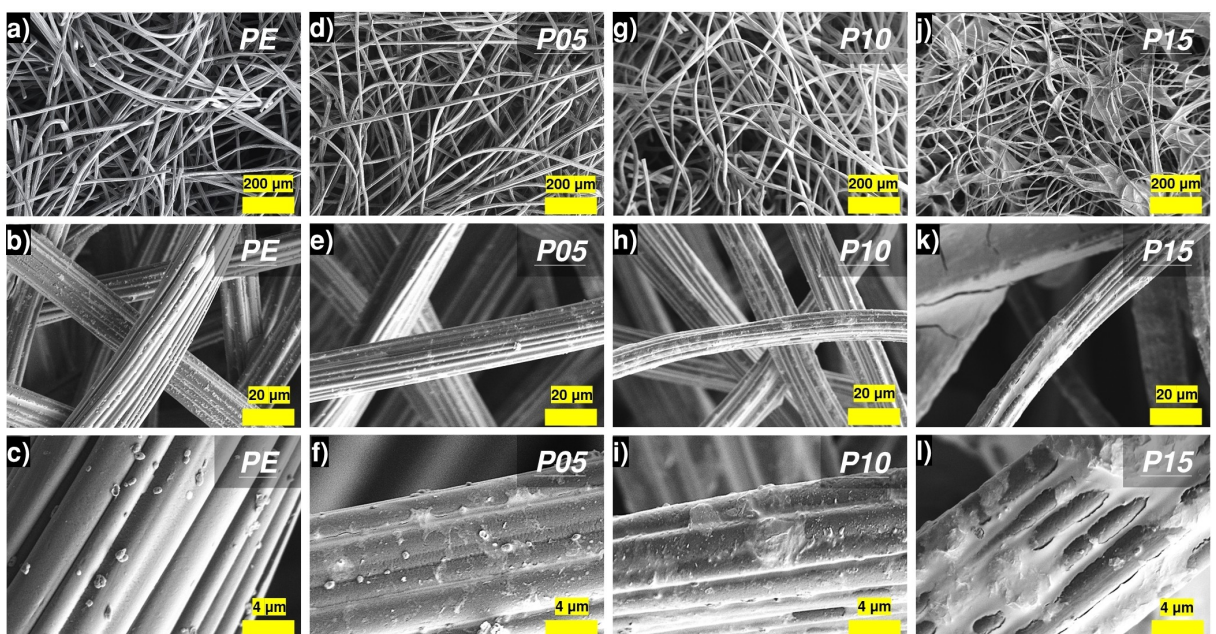


Figure 2. SEM images of the electrodes: a–c) PE; d–f) P05; g–i) P10; j–l) P15 in 100×, 1000× and 5000× magnification, respectively.

that the deposition density of the particles, and the amount of residual electrolyte on the fiber surfaces were increased with the increasing nanoparticle concentration in the nanofluidic anolytes. Especially, the grooved surface structure became mostly covered with MXene nanoparticles and residual electrolyte with the highest percentage of nano additives in the dispersion with 0.15 wt%  $Ti_3C_2T_x$  (Figure 2l). The fibers interacted with the P05 anolyte did not differ from the pristine case significantly; however, when the concentration increased to 0.10 wt% (P10), the distribution of MXene flakes on the surface of the fibers and the density of residual electrolyte were enhanced and became more observable. For the P15 anolyte, larger aggregates tended to form a rougher surface on the fibers in general, and as a result the grooved structure became less obvious. More interestingly, increased particle concentration resulted in a larger amount of remainder nanofluidic anolyte which tends to accumulate between the fibers and create obstacles to transport in the porous structure (Figure 2j and k). The electrochemically active surface area of the carbon

felt electrodes could be increased by the accumulation of  $Ti_3C_2T_x$  particles at the expense of increased pressure drop in the P15 anolyte.

## Electrochemical performance

### Polarization curves

A custom-made single cell was employed for all the flow battery tests, which presented via a schematic together with the test station (Figure 3).

For analyzing the flow battery performance of the nanofluidic anolytes, polarization curves were obtained, and accordingly, the change in overpotentials was also presented. In Figure 4(a), the polarization curves can be seen for all the anolytes. For this graph, the potential values were presented without any *iR* correction to reveal the realistic voltaic limits of each system. In contrast, Figure 4(b) omits the *iR* correction

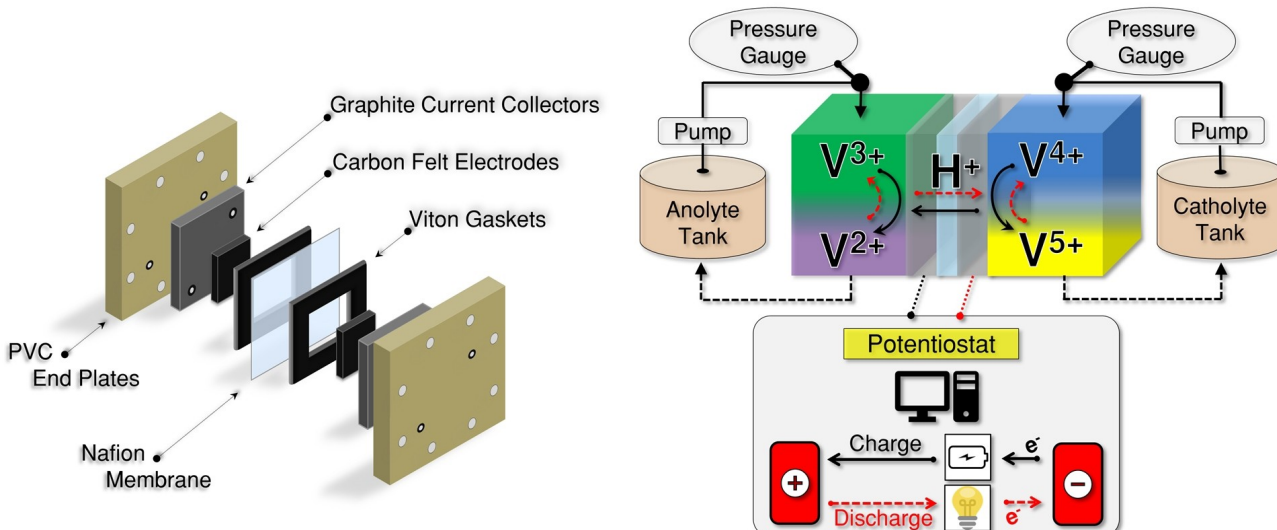


Figure 3. Schematics of the custom-made single cell flow battery and the test station.

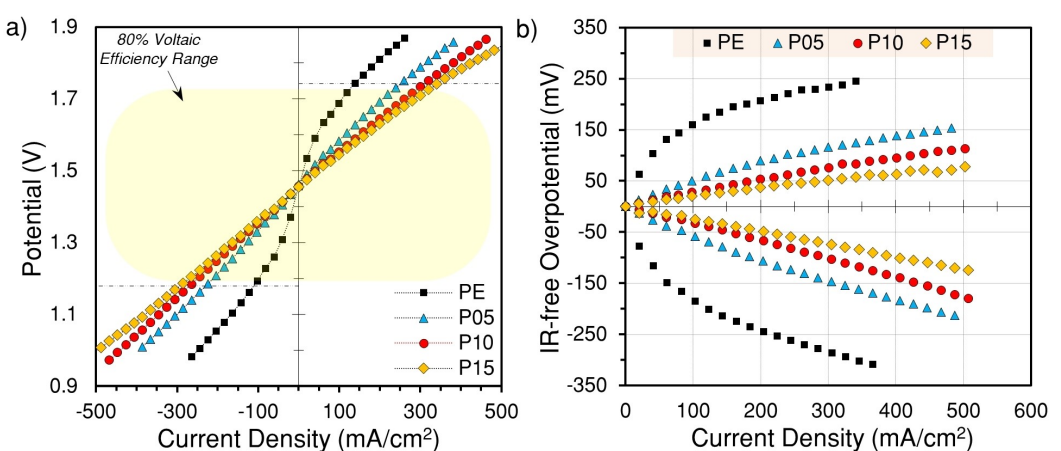


Figure 4. a) Polarization curves; b) *IR*-free overpotentials.

(ohmic losses were dismissed) to emphasize the electrochemical performance of the anolytes explicitly in terms of their kinetic properties.

It should be noted that the experiments have been set up to be ended when the voltage limits (0.5–1.8 V) were reached either at a discharging or charging step during the polarization. However, in Figure 4(a), the discharging curves do not indicate any limiting current density value because, for all the cases, the measurements were ended at the upper voltage limit of 1.8 V while a positive current was being applied. Thus, although the curves do not fully display the limiting current density values for discharging when the battery is at 50% SOC, the electrochemical performance of the anolytes could still be gathered and compared over a broad range of current densities.

As can be seen on Figure 4(a), the PE anolyte performed very poorly in the low current density region ( $\sim 250 \text{ mA cm}^{-1}$ ), indicating its insufficient kinetic activation while all other nanofluidic anolytes (P05, P10, P15) exhibited higher effectiveness for sustaining lower overpotentials for the applied charging/discharging currents. Moreover, at the current density of  $200 \text{ mA cm}^{-1}$ , the iR-free overpotentials was measured to be 207 and  $-245 \text{ mV}$  for the PE anolyte while charging and discharging, respectively (Figure 4b). However, these values were found to be 90 and  $-107 \text{ mV}$  for the electrolyte P05, which were 57% and 56% lower compared to the PE anolyte. Even though the P05 had a better performance compared to pristine anolyte, the polarization curves indicated that increased MXene concentrations in the anolytes has resulted in further decreases in the overpotentials.

Within a voltaic efficiency range of 80%, the PE electrolyte was able to be charged and discharged with the current densities of maximum  $140 \text{ mA cm}^{-1}$  and  $-120 \text{ mA cm}^{-1}$ , respectively, due to its higher activation overpotentials. On the contrary, these values were measured as 300 and  $-280 \text{ mA cm}^{-1}$  for the P10 anolyte, and in addition, as 340 and  $-300 \text{ mA cm}^{-1}$  for the P15 anolyte. The same values were recorded as 240 and  $-240 \text{ mA cm}^{-1}$  for the P05 anolyte. Even though the P05 anolyte has shown a considerable improvement in the kinetic activation, the enhancement was not as significant as compared to the other nanofluidic anolytes of P10 and P15 since both led to an increase of more than 100% compared to the PE electrolyte. The reason for the lower performance of P05 could be due to the less volumetric ratio of MXene particles in this anolyte. As can be seen in Figure 2(a), the MXene flocks were quite small in the P05 anolyte and these spheric, point-like, crumpled MXene aggregates did not generate a substantial particle network in the anolyte as the P10 and P15 anolytes did but rather established a more homogeneous distribution of isolated small MXene flocks. Consequently, the P05 anolyte was able to promote an improvement on electrochemical performance only to a certain degree. Nevertheless, the P10 and P15 anolytes have surpassed the P05 owing to their higher  $\text{Ti}_3\text{C}_2\text{T}_x$  content, which induced bigger MXene flocks to form, and established a more extensive particle network within the anolyte, thereby increasing the electrochemically active surface area.

The best performing anolytes, P10 and P15, showed similar performances at lower current densities up to  $200 \text{ mA cm}^{-1}$ . The difference in their polarization curves became more noticeable with the increasing current values. Firstly, at almost every part of the polarization curves, the P15 anolyte attained the lowest overpotentials showing superior kinetic performance. Within the experimental voltage limits, the P15 anolyte was able to reach to a current density of  $500 \text{ mA cm}^{-1}$ , and at this value, the overpotentials for charging and discharging were calculated as 77 and  $-124 \text{ mV}$ , respectively. The same values were found as 107 and  $-164 \text{ mV}$  for the P10 anolyte at the highest attained discharging current density of  $460 \text{ mA cm}^{-1}$ . In comparison, the kinetic performance of the P15 anolyte surpassed the performance of the P10 anolyte with a higher current density and even with about 30% lower overpotentials. Hence, it is obvious that increasing MXene content in anolytes further increases the electrochemical performance but there is a trade-off which is going to be more observable with the charge-discharge cycling tests. Since polarization curves were obtained at a constant 50% SOC, the difference between the mass transport behaviors of the anolytes P10 and P15 could not be distinctly identified. P15 seems to be having a better performance with lower overpotentials at almost every current density applied; however, mass transport overpotentials were not substantially affecting the formation of the polarization curves in these experimental conditions. To further evaluate the battery performances and make a more extensive comparison between each system, other tests methods are going to be discussed. Furthermore, other aspects of battery performance such as pressure drop should also be considered to make a more extensive evaluation.

### Load curves

Load curve measurements were performed at two conditions (i.e., at 50% SOC and 100% SOC) to identify the limiting current density values for each system and to observe the mass transport overpotentials (Figure 5). The SOC of the batteries was assumed to be constant during the load curve experiments even though consecutive discharge currents were only applied. Since the total time of the experiments was quite short, the change in the SOC of the batteries were considered identical for each case and thus neglected.

As can be seen in Figure 5, at both conditions, the pristine electrolyte PE exhibited the highest activation overpotential due to its limited kinetic activation. On the contrary, the nanofluidic anolytes performed superior compared to the PE anolyte. At 100% SOC, between the anolytes PE and P05, an overpotential difference of about 145 mV was recorded up until the applied current density of  $700 \text{ mA cm}^{-1}$ , which was the current limit achievable in this test station (Figure 5a). The deviation between the potential values for the P10 and P15 electrolyte was quite negligible as it was calculated at  $+/- 10 \text{ mV}$  throughout the measurements. Therefore, at the fully charged state of the batteries, the electrochemical performance

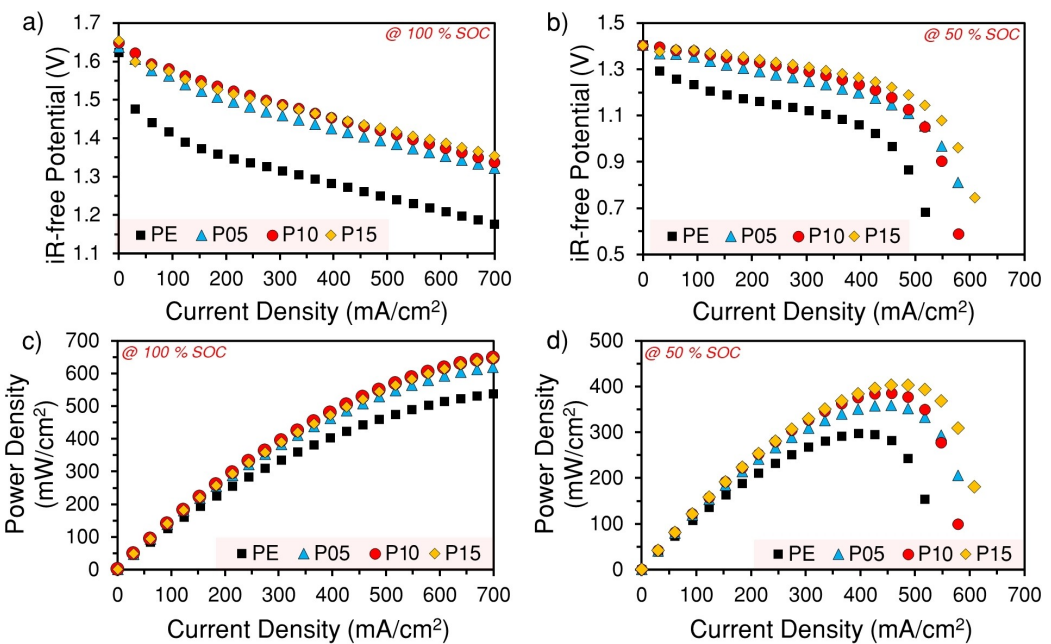


Figure 5. Load curves at a) 100% SOC; b) 50% SOC, and power density values at c) 100% SOC; d) 50% SOC.

of these two nanofluidic anolytes were found to be almost identical. However, they outperformed the P05 anolyte with an average overpotential difference of 26 mV.

Although no difference was noticed between the P10 and P15 anolytes at these experimental conditions, the disparity between their performances became more distinguishable owing to the increased mass transport overpotentials when the charge level of the batteries was dropped down to 50% SOC (Figure 5b). The reduced ratio of the active ions in the electrolytes resulted in intensified mass transport overpotentials, which prevented the batteries to be able to reach up to 700 mA cm<sup>-1</sup>. The limiting current densities for the P05 and P10 nanofluidic anolytes were recorded as 570 mA cm<sup>-1</sup>. Although the P05 showed also the same limiting current density with the P10 anolyte, its average discharge potential was much lower with a difference of 73 mV. In parallel with the polarization curves, the P05 had a better performance compared to the pristine anolyte but its improvement restrained by the limited amount of MXene addition. The volumetric equivalent of 0.05 wt% Ti<sub>3</sub>C<sub>2</sub>T<sub>x</sub> was not physically sufficient to generate a vast, web-like nanofluidic network in the anolyte (Figure 1c) when compared to the P10 and P15 anolytes.

On the other hand, the P15 anolyte had a limiting current density of 600 mA cm<sup>-1</sup>. The difference between their average discharge voltages of P10 and P15 anolytes was found as 20 mV, indicating a small variation. Likewise, the limiting current densities were close to each other with about a 5% difference. Hence, the performances of these two anolytes did not significantly differ from each other. But the mass transport capacity of the P15 anolyte is slightly better compared to the P10 anolyte, which was also affirmed by the charge-discharge cycling results that are discussed in the next section.

The power density values were also calculated based on the load curves Figure 5(c and d). At the highest current density of 690 mA cm<sup>-1</sup>, owing to their substantial kinetic improvements, the P10 and P15 anolytes were able to achieve the power densities of 648 and 646 mW cm<sup>-1</sup>, respectively. Compared to the pristine electrolyte that attained a power density of 538 mW cm<sup>-1</sup> at the same current density, these values indicated about 20% improvement. At 50% SOC, the P15 anolyte had a maximum power density of 403 mW cm<sup>-1</sup> at 480 mA cm<sup>-1</sup> while P1 reached 385 mW cm<sup>-1</sup> at the current density of 450 mA cm<sup>-1</sup> (Figure 5d). Only about 5% improvement in the maximum power density value was calculated, indicating that at the low charge states, the P15 anolyte could not considerably outperform the P10 anolyte. At the same conditions, the pristine anolyte was able to reach only to a maximum power density of 298 mW cm<sup>-1</sup> at 390 mA cm<sup>-1</sup>. Consequently, the polarization and load curve measurements indicated that the P10 and P15 MXene added nanofluidic anolytes exhibited a quite favorable kinetic improvement due to enhanced electrocatalytic activity and increased electrochemically active surface area provided by the crumpled MXene nano particles. Nevertheless, the increased hydraulic effects hamper the advantages of the P15 anolyte because of the extravagantly intensified pumping loads, which is discussed extensively in the *hydraulic effects* section.

Lastly, the limited performance of the P05 anolyte and the performance difference in the nanofluidic anolytes indicate that nanofluidic systems are functioning over certain factors. The size and the distribution of the additive particles play a significant role by increasing the active surface area, which facilitates the electrode kinetics; however, if the volumetric distribution of additive material is not enough to create an extensive network of particles, the performance can only

improve to a certain degree. Likewise, volumetric distribution of the nanofluidic particles should also be regulated with the increasing amount of additive material due to the limitations exerted by the properties of porous media (i.e., pore density, average pore size and tortuosity of electrodes) and their interactions with the nano particles.

### EIS analysis

In addition to the other battery tests, EIS was also performed to analyze the kinetics of each anolyte, and the Nyquist plots are presented in Figure 6. The values on the x-axis were offset regarding the ease of comparison between each other; however, the deviations were so minor that only caused by the ohmic resistances due to the connections. In the high frequency region of the Nyquist plots, the first interception of the semi-circle at the x-axis gives the value for the ohmic resistances relating to the losses caused by the electronic and ionic transport mechanisms throughout the battery while the diameter of the semi-circle gives the impedance value for the charge transfer kinetics.

First, after introducing the nanofluidic anolytes to the batteries, the diameter of the semi-circles started to decrease. At the static condition, the semi-circle for the PE anolyte at the high frequency region had a diameter of 0.166 ohm, and it dropped to 0.083 ohm for the P05 anolyte. Moreover, the same values for the Nyquist plots of the P10 and P15 anolytes further dropped to 0.048 and 0.043 ohm, respectively. In parallel with the polarization curves and efficiency calculations, the MXene addition to the anolytes has enhanced the reaction kinetics, and charge transfer resistances decreased by 74% when the PE and P15 anolytes are compared. At the low frequency region of the Nyquist plots, the slopes of the linear tails were gradually increasing with the amount of MXene particles in the anolytes. The slopes were approximately 6.35, 8.26, 9.54, and 9.86 for the PE, P05, P10 and P15 anolytes, respectively. This increasing trend in the slopes may indicate enhancement in the capacitive behavior due to the increased physical surface area by the

added  $Ti_3C_2T_x$  particles. In the dynamic condition, the overall behaviors were similar to the static condition at zero flow rate. However, a slight decrease in the impedances was observed. The P10 and P15 anolytes had almost the same charge transfer resistances at both conditions. Under the static condition, the difference in their kinetic behavior was 0.005 Ohm and it was 0.001 Ohm at the dynamic condition.

### Charge-discharge cycling and long-term stability

To further investigate the performance of the MXene added nanofluidic anolytes, charge-discharge cycling tests were conducted at various current densities (i.e., 50, 100, 150, and  $200\text{ mA cm}^{-2}$ ), and the results are shown in Figure 7. Based on the data collected during the charge-discharge cycles at these current densities, coulombic efficiency, voltaic efficiency, and energy efficiency values were calculated and presented together with the discharge capacities and the depth of discharge rates (DoD) in Figure 8. A more detailed presentation on the calculated values were exclusively displayed on Table S1. The DoD rates were found by calculating the ratio of the number of charges that passed through the circuit during a discharge step to the theoretical total number of charges in an anolyte with a volume of 20 mL containing 1 M concentration of vanadium salts.

In accordance with the polarization data, the PE electrolyte exhibited the highest overpotentials, and with the increasing current densities, the electrolyte utilization rates showed a very steep decline due to its insufficient kinetic activity and mass transport capability (Figure 7). In general, the PE electrolyte had the most limited capacity utilization along with the lowest voltaic efficiencies as expected. On the other hand, the nanofluidic anolytes have considerably improved the capacity utilizations along with the voltaic efficiencies due to their lower activation overpotentials at both charging and discharging. At the linear parts of the plots, the P10 and P15 anolytes have shown a similar behavior with duplicating voltage values, which can also be seen in the voltaic efficiencies in Table S1

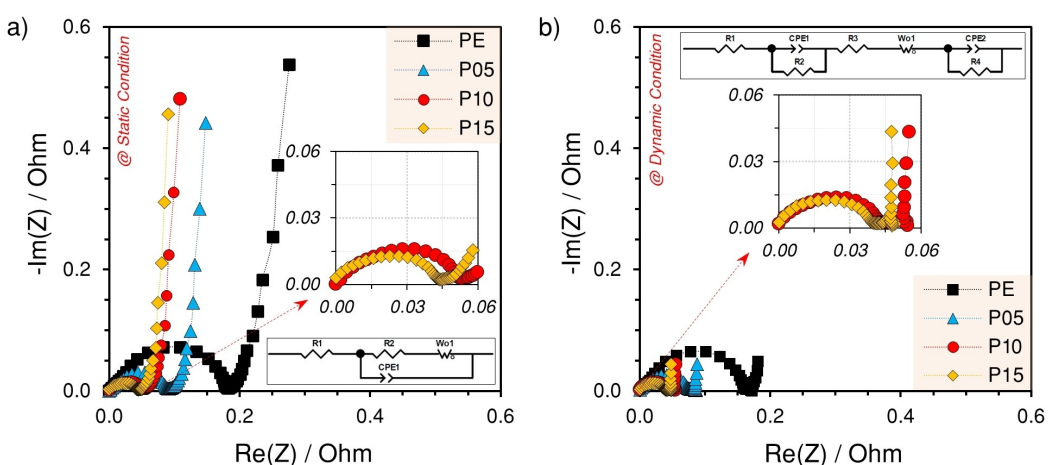
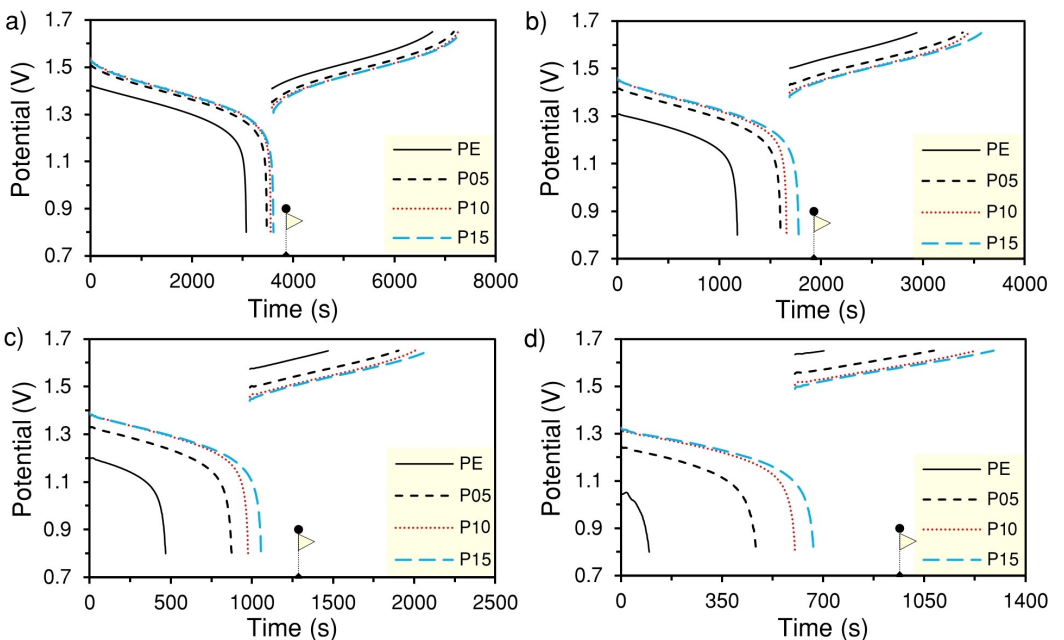
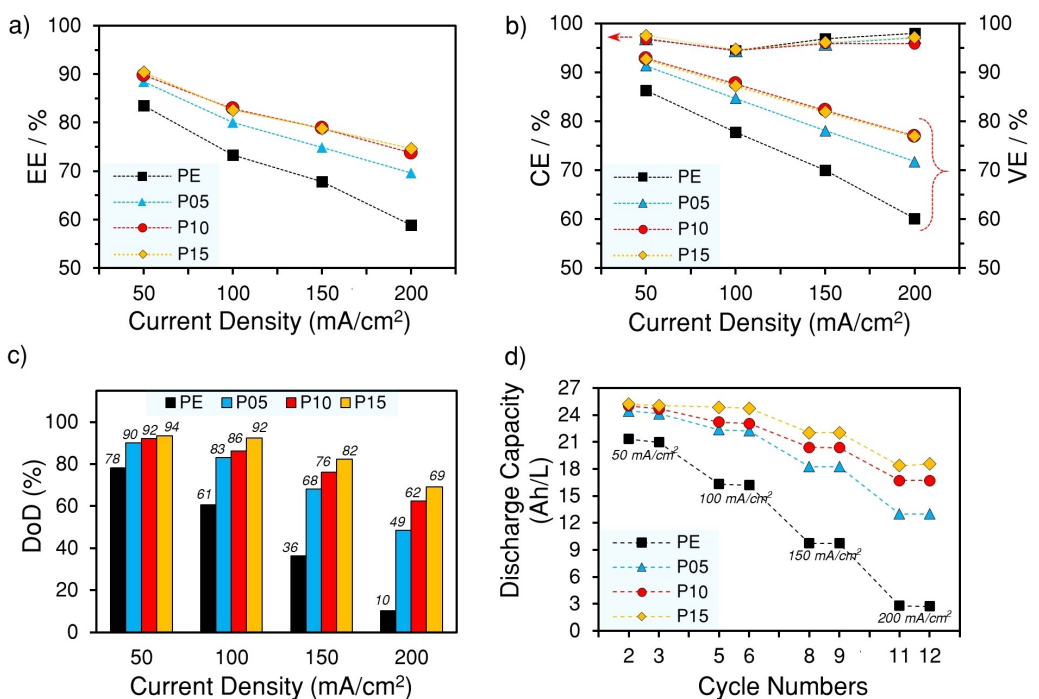


Figure 6. Nyquist plots for a) the static condition and for b) the dynamic condition.



**Figure 7.** Charge-discharge cycles at a) 50 mA cm<sup>-2</sup>; b) 100 mA cm<sup>-2</sup>; c) 150 mA cm<sup>-2</sup>; and d) 200 mA cm<sup>-2</sup>. The yellow flag represents the theoretical discharge capacity.



**Figure 8.** a) Depth of discharge (DoD) rates at different current densities; b) discharge capacities; c) energy efficiencies; and d) coulombic and voltaic efficiencies.

and Figure 8(b). But, with the increasing current densities, the discharge capacity of the P15 anolyte started to exceed the P10 anolyte. This is in correlation with the polarization curve measurements (Figure 4), in which the increasing current densities resulted in higher overpotentials for the P10 anolyte and increased current densities has resulted in more difference in their electrochemical performance.

Interestingly, even though the P15 anolyte caused excessive pressure drops, the mass transport overpotentials did not seem to be affected as the P10 anolyte. This can be attributed to the structural advantages of 3 mm thick carbon felt electrodes, which were not as susceptible to be clogged as very thin carbon paper electrodes.<sup>[42]</sup> Thus, the decreased activation overpotentials have been partially counterbalanced with the

enlarged mass transport overpotentials caused by the excessive MXene in the anolytes, but the former was more dominant, and the latter has proposed itself mostly as adverse hydraulic effect. In addition, due to this trade-off, a saturation point was reached, and increasing the MXene portion in anolyte would not increase the electrochemical performance further and would result in more aggravated pressure drops. Moreover, the calculations indicate that the efficiency values were found to be same for the P10 and P15 anolyte (Table S1), suggesting the trade-off limits further enhancements in the performances.

The energy efficiencies of the electrolyte PE were calculated as 84%, 73%, 68% and 59% with the increasing current densities (Figure 8a) while the P05 anolyte had higher efficiencies (88%, 80%, 75%, and 70%) in the same conditions (Table S1). In parallel with the polarization results, the P1 and P15 anolytes showed the same efficiencies with insignificant deviations. During the cycling tests, they both had the same energy efficiencies of 90%, 83%, 79% and 74%–75% at the increasing currents. Although, compared to the PE anolyte, the P10 and P15 anolytes improved the efficiencies by 7%, 11%, 16%, and 25%, a more comprehensive understanding on the anolyte performances can be deduced by comparing the DoD rates of each system as it was clearly demonstrated in Figure 8(c). Even though the PE anolyte seemed to have moderate energy efficiency values in the studied current density region, its utilization was severely restrained with the increasing current densities because of its higher activation and mass transport overpotentials.

At the highest current density of  $200 \text{ mA cm}^{-2}$ , the DoD rate of the PE anolyte has dropped severely down to 10%. Nevertheless, at the same current density, the nanofluidic P05, P10, and P15 anolytes were able to utilize 49%, 62% and 69% of their theoretical capacities, respectively. In addition, the discharge capacities were calculated and presented for every 2<sup>nd</sup> and 3<sup>rd</sup> cycle of the experiments (Figure 8d). As the experiments were started from a fully charged state, the first cycles of the experiments were not presented in the graphs for the sake of clarity. Compared to the other cases, the P15 anolyte showed the highest capacity utilization at all current densities, and it also had a smaller capacity drop rate at the elevated current loads. With the increasing current densities, the P15 anolyte had the discharge capacities of 25.1, 24.8, 22, and  $18.6 \text{ Ah L}^{-1}$  while the P10 anolyte was able to reach lower discharge capacities of 24.7, 23.1, 20.4, and  $16.76 \text{ Ah L}^{-1}$ . Contrarily, the PE anolyte showed a very sharp decline in the capacity utilization due to the tremendously enhanced kinetic overpotentials with the increasing current densities, which was also because the PE anolyte showed more susceptibility to the mass transport limitations (Figure 5b). Compared to the PE anolyte, P05 had a better performance with higher discharge capacities; nevertheless, the P10 and P15 anolytes surpassed the performance of the P05, which was in parallel to the other flow battery test results.

In general, the P15 anolyte showed the best performance and reached to higher electrolyte utilization rates. The improved performance of the P15 anolyte can be attributed to the enhanced kinetic performance and the electrochemically

active surface area. As a nanofluidic additive, well-dispersed, independent MXene particles created spontaneous, and dynamic web-like surfaces that facilitated the anodic  $\text{V}^{2+}/\text{V}^{3+}$  redox reactions owing to the increased electrochemically active surface area and enhanced reaction kinetics. Nevertheless, pressure drop, being one of the most crucial parasitic losses in flow batteries, should also be considered to fully comprehend the overall effect of MXene addition to the anolyte in terms of feasibility.

The long-term stability is a very crucial aspect of an electrochemical system. To analyze the stability of the nanofluidic electrolytes, 300 cycles were run with the P10 anolyte and the corresponding energy, coulombic, and voltaic efficiencies were shown in Figure S2(a) together with the change in the discharge capacities in Figure S2(b). The cycling has been conducted at the current density of  $200 \text{ mA cm}^{-2}$ . The initial and final discharge capacities over 300 cycles were found to be 14.5 and  $10.8 \text{ Ah L}^{-1}$ , respectively. This calculation indicates that the total capacity decay would be 25.7% for 300 cycles, and the average discharge capacity fade rate can be calculated as about 0.09% per cycle, which was mainly because of the crossover of active species through the Nafion membrane.<sup>[46,47]</sup> However, even though there was an inevitable capacity fade due to the crossover, no observable decays have been observed with the calculated efficiencies indicating remarkable stability needed for long-term operations.

### Hydraulic effects

To fully comprehend the effect of nanofluidic anolytes on the overall battery performance, pressure drop measurements were carried out. Crucial information on how the particle addition influenced the hydraulic performance of the anode pressure can be seen on the Figure 9. The pressure drops were measured at six different flow rates for five minutes at 50% SOC, and the recorded pressure values were averaged. The cathodic pressure drops were not measured, as the focus of the experiments were on the hydraulic effect of the nanofluidic anolytes. The measurements represent the overall pressure drop that are associated with a complete single cell flow battery stack, which included the fittings, end plates and the electrodes, along with the anolytes. Nevertheless, the change in the pressure drops can be attributed to the effect of the added MXene in the anolytes since all the other factors stayed constant for all the measurements.

As can be seen in Figure 9, the PE anolyte showed the least pressure drops at all flow rates as expected. The graph for the PE anolyte had a slope of 0.24. The baseline values were measured for the PE anolyte as 6, 11, 16, 21, 26 and 29 kPa. Compared to the PE anolyte, the nanofluidic anolytes had higher pressure drops in general. The pressure drop measured at  $20 \text{ mL min}^{-1}$  for the P05 and P10 anolytes was 9 kPa, which was 50% higher than the PE anolyte. The P05 and P1 had almost the same pressure drops at the lower flow rates with only insignificant deviations since the slopes of their trendlines were almost identical. At the flow rates of 20, 40 and

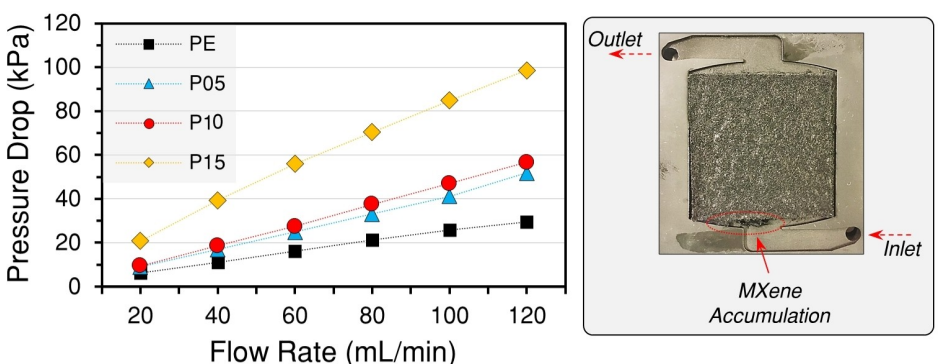


**Figure 9.** Pressure drops for various flow rates, and the image showing the MXene accumulation on the side of the carbon felt electrode at the inlet.

60  $\text{mL min}^{-1}$ , the P05 and P10 anolytes had the pressure drop values of 9, 17 and 25 kPa, and 9, 19 and 27 kPa, respectively. The difference in their pressure drops became more distinguished at the higher flow rates. At the flow rates of 100 and 120  $\text{mL min}^{-1}$ , the P1 anolyte showed the pressure drops of 47 and 57 kPa, which were 14 and 9% higher than the P05 anolyte (41 and 52 kPa). Moreover, when P10 anolyte is compared to the PE for all the test conditions (i.e., the flow rates of 20, 40, 60, 80, 100 and 120  $\text{mL min}^{-1}$ ), the increases in the pressure drops were observed to be 50, 69, 72, 77, 81 and 92%, respectively.

On the other hand, the P15 anolyte showed the most severe pressure drops compared to all the other cases. Even its baseline value at the lowest flow rate of 20  $\text{mL min}^{-1}$  was measured as 21 kPa, which was 250% higher than the pressure drop observed for the PE anolyte. This value was also 62% higher than the P10 anolyte. The linear trendline for the pressure drop measurements of the P15 anolyte had a slope of 0.77, and due to the highest baseline value together with its much steeper slope, the P15 had the most aggravated pressure drop at every flow rates. At the highest flow rate of 120  $\text{mL min}^{-1}$ , the pressure drop was 99 kPa for the P15 anolyte and the difference between the P10 and P15 anolyte was calculated as 74%. When it was compared to the PE anolyte, the difference was 235%. The vastly intensified pressure drops can be attributed to the increased concentration of nano particles in the anolytes, which started to form flocks that were big enough to hinder the electrolyte penetration and intrusion through the porous structure. For the P05 and P10 anolytes, even though the pressure drops were observed to be increasing, the concentrations of MXene in these anolytes did not cause a strongly adverse hydraulic effect. Furthermore, such intensified pressure drop values may hamper the suitability of practical applications for the P15 anolyte despite its superior electrochemical performance.

## Conclusion

In this study, we have shown that MXene added nanofluidic anolytes enhances the electrode kinetics and helps in facilitating the anodic  $\text{V}^{2+}/\text{V}^{3+}$  redox reactions. The improvement in

the electrochemical performance realized by the utilization of nanofluidic anolytes is observed to be tantamount to direct surface treatment of pristine electrodes. Moreover, the nanofluidic electrolytes improve the mass transport capacity of carbon felt electrodes by creating a dynamic, web-like structure in anolytes, which mainly performs as a flowing electrode creating more electrochemically active surfaces in the pores of carbon felt electrode. A facile preparation method was used to prepare the nanofluidic anolytes. The optimal additive MXene concentration in the anolyte was 0.10 wt% (P10). At this concentration, electrochemical performance of the VRFB has shown much better improvement due to the highly reduced activation overpotentials, and more importantly, along with the enhanced electrocatalytic activity,  $\text{Ti}_3\text{C}_2\text{T}_x$  has not created adverse hydraulic effects in the P10 anolyte while the P15 anolyte with a MXene concentration of 0.15 wt% caused severe pressure drops.

Within a voltaic efficiency range of 80%, the P10 anolyte achieved the maximum charging and discharging current densities of 300 and  $-280 \text{ mA cm}^{-2}$ , respectively. Compared to the pristine anolyte, these values were increased by 114% for charging and 133% for discharging. At the 50% and 100% SOC, the P10 anolyte had a power density of 385 and 648  $\text{mW cm}^{-2}$ , respectively. During the charge-discharge cycling, at the highest current density of 200  $\text{mA cm}^{-2}$ , the P10 anolyte had a DoD rate of 62%, which was about 600% higher than the capacity utilization of the pristine anolyte. Furthermore, at the same current density, with an increase of 28% compared to the pristine anolyte, the P10 anolyte had an energy efficiency of 77%. Moreover, it also showed remarkable stability over 300 cycles with a significant capacity retention rate, and no efficiency decay at a current density of 200  $\text{mA cm}^{-2}$ . Lastly, the hydraulic effect seemed to be exacerbated to a tolerable extent with the P10 anolyte. At a relatively high flow rate of 120  $\text{mL min}^{-1}$ , its pressure drop rose to 57 kPa with an increase of 97% compared to the pristine anolyte. On the contrary, at the lowest flow rate of 20  $\text{mL min}^{-1}$ , the P15 anolyte had an acutely aggravated pressure drop of 21 kPa with an increase of 250%, which indicates a concentration limit for the nanofluidic additives where detrimental hydraulic effects start hampering the utilization of nanofluidic

anolytes. Therefore, more studies are needed to address particle agglomeration and subsequent pressure drop.

## Experimental Section

**MXene synthesis:** Synthesis of  $Ti_3C_2T_x$  MXene was adopted from the literature.<sup>[43]</sup>  $Ti_3AlC_2$  MAX precursor was synthesized by mixing  $TiC$ ,  $Ti$ , and  $Al$  powders (2:1:1 mass ratio) via ball milling, followed by annealing at 1380 °C for 2 h under argon (Ar) atmosphere. The obtained MAX phase was washed with 9 M HCl overnight to remove the intermetallic phases, and the particles below 38  $\mu m$  were separated.  $Ti_3C_2T_x$  MXene was synthesized by adding 1 g of the MAX precursor to the etching solution containing a mixture of HF (49%, 2 mL), HCl (36%, 12 mL), and  $H_2O$  (DI, 6 mL). The reaction was allowed to stir for 24 h at 35 °C. The resultant multilayer MXene powder was washed with water until neutral pH, then delaminated using 1 g of LiCl in 50 mL of water for 18 hours at room temperature. To remove LiCl from the solution, the mixture was centrifuged for 5 min at 3500 rpm, and the clear supernatant was discarded. The MXene powder was redispersed in water and centrifuged again for 1 hour, discarding the supernatant again. For the following centrifugation cycles, the MXene was redispersed in water and centrifuged for 15 min at 3500 rpm while collecting the dark supernatant, which contains single-layer MXene flakes. For the last step, the single-layer MXene solution was concentrated using high-speed centrifugation (10 min, 10000 rpm) and stored in an Ar-sealed vial in a refrigerator until further use.

**Nanofluidic anolyte synthesis:** A monodispersed  $Ti_3C_2T_x$  suspension with a concentration of 8 mg  $cm^{-3}$  was used for nanofluidic anolyte preparation. The procedure was started as if a regular vanadium electrolyte (1 M vanadium – 4 M  $H_2SO_4$ ) was being synthesized.<sup>[48]</sup> The calculated amount of vanadium (IV) oxide sulfate hydrate ( $VOSO_4 \cdot xH_2O$  – 97%, Sigma Aldrich) was initially added to deionized (DI) water at about 75 °C, and then concentrated sulfuric acid ( $H_2SO_4$  – 96.3%, Sigma Aldrich) was slowly added to the solution while stirring vigorously. However, the necessary amount of DI water to obtain the intended concentration was deliberately curtailed to be able to add the required amount of MXene dispersion later. Afterwards, the solution was continued to be moderately stirred overnight, and the temperature was kept approximately at 40 °C to guarantee that vanadium salts were fully dissolved. Consecutively, the volume of the anolytes was rounded up to 40 mL by adding the necessary amount of MXene dispersion and DI water with a micropipette based on the numerical calculations. Afterwards, to minimize the oxidation of delaminated MXene nanoflakes in the solution, the electrolytes were purged with nitrogen gas ( $N_2$ ) for 15 minutes. Lastly, the mixture was vigorously stirred with a magnetic stirrer for 24 hours to obtain homogeneous and stable  $Ti_3C_2T_x$  suspensions. Finally, four different weight percentages of  $Ti_3C_2T_x$  were acquired as 0, 0.05, 0.10, and 0.15 wt% and labeled as PE, P05, P10, and P15, respectively.

**Flow battery testing setup:** A custom-made single cell was employed for the flow battery tests (Figure 3). Two graphitic current collectors together with square carbon felts (SGL - GDA3) with a thickness of 3 mm, and with a geometric surface area of 10  $cm^2$  used on both sides. The cell was separated with a Nafion 212 (Dupont) membrane, and the components were sandwiched between PVC endplates. The compression was achieved by uniformly applying a torque of 15 in-lbs. on six stainless-steel screws, and the compression rate was maintained at ~30% via Viton rubber gaskets. Peristaltic pumps (Cole Palmer) were used to transfer the electrolytes into the cell by Tygon tubing (Saint-Gobain). The pressure gauges were attached close to the inlets on both sides of the battery. For precharging, a volume of 20 mL for

anolyte and catholyte was employed on each side of the battery, where the catholyte contained 0 wt%  $Ti_3C_2T_x$  (i.e., the PE electrolyte) to avoid chemical instability under positive potentials. To maintain the charge balance and ensure the full conversion from V(IV) to V(II) in the anode side, the starting volume of the catholyte was established as 40 mL during the precharging stage, and after the cell had reached to 100% state of charge (SOC) level, half of the catholyte was removed from the tank. The electrolytes and the reservoirs were purged with  $N_2$  for 45 minutes prior to flow tests, and air was prevented from diffusing into the tanks with a constant  $N_2$  blanket sustained for the duration of the experiments. Throughout the flow battery experiments, the flow rate was maintained at 50  $mL\min^{-1}$  except during the EIS measurements in static condition at which the electrolyte flow was interrupted.

**Electrochemical characterization and flow battery tests:** The flow battery experiments were carried out with a Scribner Associates 857 redox flow cell test system and the EIS data was collected with the BioLogic VMP multichannel potentiostat. After completing the precharging procedure, load curves were obtained first at 100% SOC before initiating the charge-discharge cycling experiments. With an increment of 30  $mA\text{cm}^{-2}$ , an increasing discharge current was applied for 8 seconds at every step and four data points were collected. In contrast to polarization measurements, there was no charging current applied between discharging steps. The SOC of the batteries was altered during this period, but it was assumed that the change was identical for every case and can be ignored. Afterwards, the charge-discharge cycling tests were conducted at four different current densities (50, 100, 150, and 200  $mA\text{cm}^{-2}$ ) to analyze the operational performance of each battery setup. To eliminate side reactions, the upper voltage limit during charging was maintained at 1.65 V, and the lower limit was maintained at 0.8 V. After the charge-discharge cycling measurements, the battery was fully charged and then discharged to 50% SOC to obtain the polarization curves at this charge level. The tests were performed at constant 50% SOC level, which was assumed to be an average charge level of an operating battery. The open-circuit-voltage (OCV) values were measured to ensure that a constant SOC at 50% was maintained during the tests, and the pre- and post-evaluations of the OCVs affirmed that the values always remained within a range of 5 mV ( $\approx 1.41$  V). To acquire polarization data, a series of galvanostatic charge and discharge steps with a gradient of 20  $mA\text{cm}^{-2}$  were applied for 20 seconds until reaching the limiting voltage values. For every current step, 10 corresponding potential values were averaged and recorded. Moreover,  $iR$ -corrected values were also reported to explicitly diagnose overpotentials relating to the kinetics and mass transport properties of the anolytes. Following the polarization tests, EIS measurements were conducted at the same SOC level of 50%. All tests were potentiostatically controlled with a magnitude of 50 mV between the frequencies of 0.5 mHz and 100 kHz. The working electrode was set as the cathode while the reference and counter electrodes were set as the anode. EIS measurements were performed both at static (0  $mL\text{ min}^{-1}$ ) and flow conditions (50  $mL\text{ min}^{-1}$ ). Lastly, pressure drop measurements were carried out at six different flow rates (20, 40, 60, 80, 100, and 120  $mL\text{ min}^{-1}$ ). For each flow rate, the measurement was performed for 5 minutes, and the pressure drop data was recorded at every 2 seconds, and the averages were calculated.

**Material characterization:** The prepared MXene solution was measured by dynamic light scattering (DLS, Malvern Instruments, USA) to analyze its flake size distribution. For evaluating the flake size, about 1 mL of diluted MXene dispersion was introduced into a polymer holder, and three measurements were carried out in total. Transmission electron microscopy (TEM) and selected area electron diffraction (SAED) were performed on a JOEL 2100F field emission

microscope operated at an accelerating voltage of 200 kV. The dilute solution of freshly prepared MXene was drop casted out of water onto copper grids coated with a carbon film. For atomic force microscopy (AFM), a dilute solution of MXene was drop casted on a silicon substrate with 280 nm wet thermal oxide (University Wafers). The measurements were performed using Bruker Multimode 8 instrument with a Si tip (Budget Sensors Tap300Al-G) in a tapping mode in air. Lastly, for scanning electron microscopy (SEM) a Zeiss Supra 50 VP microscope was utilized to understand the morphological characteristics of the fibers of carbon felt electrodes. After the flow battery tests, electrode samples were cut, washed with DI water, and air-dried. The images were captured at 100 $\times$ , 1000 $\times$  and 5000 $\times$  magnifications. To investigate the effect of low-pH environment on  $Ti_3C_2T_x$  flakes, the MXene solution was added to the plain electrolyte solution (PE) containing 1 M vanadium salt and 4 M sulfuric acid, washed to neutral pH, and freeze-dried. Lastly, the crumpled MXene particles were deposited onto a Si/SiO<sub>2</sub> substrate for SEM imaging.

## Acknowledgements

The authors would like to thank the National Science Foundation (Grant # 2034108) for supporting this work. Research on electrochemistry of MXenes was supported by the Fluid Interface Reactions, Structures, and Transport (FIRST) Center, an Energy Frontier Research Center funded by the US Department of Energy, Office of Science, and Office of Basic Energy Sciences.

## Conflict of Interest

The authors declare no conflict of interest.

## Data Availability Statement

The data that support the findings of this study are available from the corresponding author upon reasonable request.

**Keywords:** electrochemistry • nanofluidic electrolytes • nanoparticles • MXene • vanadium flow batteries

- [1] T. M. Gür, *Energy Environ. Sci.* **2018**, *11*, 2696–2767.
- [2] G. Papaefthymiou, K. Dragoon, *Energy Policy* **2016**, *92*, 69–82.
- [3] L. F. Arenas, C. Ponce de León, F. C. Walsh, *J. Energy Storage* **2017**, *11*, 119–153.
- [4] M. Skylas-Kazacos, C. Menictas, T. Lim, in *Electricity Transmission, Distribution and Storage Systems* (Ed.: Z. Melhem), Woodhead Publishing, 2013, pp. 398–441.
- [5] M. Skylas-Kazacos, M. Rychcik, R. G. Robins, A. G. Fane, M. A. Green, *J. Electrochem. Soc.* **1986**, *133*, 1057–1058.
- [6] K. Lourenssen, J. Williams, F. Ahmadpour, R. Clemmer, S. Tasnim, *J. Energy Storage* **2019**, *25*, 100844.
- [7] K. Mongird, V. V. Viswanathan, P. J. Balducci, M. J. E. Alam, V. Fotedar, V. S. Koritarov, B. Hadjerioua, *Energy Storage Technology and Cost Characterization Report*, United States, **2019**.
- [8] M. Taş, G. Elden, *Energy Storage* **2021**, *4*, e265.
- [9] B. Akuzum, Y. C. Alparslan, N. C. Robinson, E. Agar, E. C. Kumbur, *J. Appl. Electrochem.* **2019**, *49*, 551–561.
- [10] C. R. Dennison, E. Agar, B. Akuzum, E. C. Kumbur, *J. Electrochem. Soc.* **2015**, *163*, A5163–A5169.
- [11] D. Chen, M. A. Hickner, E. Agar, E. C. Kumbur, *J. Membr. Sci.* **2013**, *437*, 108–113.
- [12] S. Tushima, T. Suzuki, *J. Electrochem. Soc.* **2020**, *167*, 020553.
- [13] H. Chen, M. Cheng, X. Feng, Y. Chen, F. Chen, J. Xu, *J. Power Sources* **2021**, *515*, 230606.
- [14] K. Yaji, S. Yamasaki, S. Tushima, T. Suzuki, K. Fujita, *Struct. Multidiscipl. Optim.* **2018**, *57*, 535–546.
- [15] C. Choi, S. Kim, R. Kim, Y. Choi, S. Kim, H.-y. Jung, J. H. Yang, H.-T. Kim, *Renewable Sustainable Energy Rev.* **2017**, *69*, 263–274.
- [16] M. Skylas-Kazacos, L. Cao, M. Kazacos, N. Kausar, A. Mousa, *ChemSusChem* **2016**, *9*, 1521–1543.
- [17] S. Xiao, L. Yu, L. Wu, L. Liu, X. Qiu, J. Xi, *Electrochim. Acta* **2016**, *187*, 525–534.
- [18] L. Cao, M. Skylas-Kazacos, C. Menictas, J. Noack, *J. Energy Chem.* **2018**, *27*, 1269–1291.
- [19] R. Saidur, K. Y. Leong, H. A. Mohammed, *Renewable Sustainable Energy Rev.* **2011**, *15*, 1646–1668.
- [20] A. R. I. Ali, B. Salam, *SN Applied Sciences* **2020**, *2*, 1636.
- [21] E. C. Okonkwo, I. Wole-Osho, I. W. Almanassra, Y. M. Abdullatif, T. Al-Ansari, *J. Therm. Anal. Calorim.* **2021**, *145*, 2817–2872.
- [22] M. Duduta, B. Ho, V. C. Wood, P. Limthongkul, V. E. Brunini, W. C. Carter, Y.-M. Chiang, *Adv. Energy Mater.* **2011**, *1*, 511–516.
- [23] K. B. Hatzell, M. Boota, E. C. Kumbur, Y. Gogotsi, *J. Electrochem. Soc.* **2015**, *162*, A5007–A5012.
- [24] J. Lobato, E. Mena, M. Millán, *ChemistrySelect* **2017**, *2*, 8446–8450.
- [25] J. Kim, H. Park, *Energy Storage* **2019**, *1*, e90.
- [26] J. Kim, H. Park, *J. Power Sources* **2021**, *500*, 229974.
- [27] J. Kim, H. Park, *J. Energy Storage* **2021**, *38*, 102529.
- [28] S. Aberoumand, P. Woodfield, G. Shi, T. Kien Nguyen, H.-Q. Nguyen, Q. Li, B. Shabani, D. Viet Dao, *J. Mol. Liq.* **2021**, *338*, 116860.
- [29] S. Aberoumand, D. Dubal, P. Woodfield, K. Mahale, H. D. Pham, C. Padwal, T. Tung, M. J. A. Shiddiky, D. V. Dao, *J. Energy Storage* **2022**, *49*, 104133.
- [30] B. Anasori, M. R. Lukatskaya, Y. Gogotsi, *Nat. Rev. Mater.* **2017**, *2*, 16098.
- [31] V. Natu, M. Clites, E. Pomerantseva, M. W. Barsoum, *Mater. Res. Lett.* **2018**, *6*, 230–235.
- [32] S. Uzun, M. Schelling, K. Hantanasisirakul, T. S. Mathis, R. Askeland, G. Dion, Y. Gogotsi, *Small* **2020**, *17*, 2006376.
- [33] S. Uzun, M. Han, C. J. Strobel, K. Hantanasisirakul, A. Goad, G. Dion, Y. Gogotsi, *Carbon* **2021**, *174*, 382–389.
- [34] L. Agartan, K. Hantanasisirakul, S. Buczek, B. Akuzum, K. A. Mahmoud, B. Anasori, Y. Gogotsi, E. C. Kumbur, *Desalination* **2020**, *477*, 114267.
- [35] Y.-Y. Peng, B. Akuzum, N. Kurra, M.-Q. Zhao, M. Alhabeb, B. Anasori, E. C. Kumbur, H. N. Alshareef, M.-D. Ger, Y. Gogotsi, *Energy Environ. Sci.* **2016**, *9*, 2847–2854.
- [36] P. Forouzandeh, S. C. Pillai, *Curr. Opin. Chem. Eng.* **2021**, *33*, 100710.
- [37] J. Huang, Z. Li, Y. Mao, Z. Li, *Nano Select* **2021**, *2*, 1480–1508.
- [38] Y.-Z. Zhang, J. K. El-Demellawi, Q. Jiang, G. Ge, H. Liang, K. Lee, X. Dong, H. N. Alshareef, *Chem. Soc. Rev.* **2020**, *49*, 7229–7251.
- [39] A. Szuplewska, D. Kulpińska, A. Dybko, M. Chudy, A. M. Jastrzębska, A. Olszyna, Z. Brzózka, *Trends Biotechnol.* **2020**, *38*, 264–279.
- [40] X. Li, Y. Bai, X. Shi, N. Su, G. Nie, R. Zhang, H. Nie, L. Ye, *Mater. Adv.* **2021**, *2*, 1570–1594.
- [41] M. Xin, J. Li, Z. Ma, L. Pan, Y. Shi, *Front. Chem.* **2020**, *8*.
- [42] A. V. Mizrak, S. Uzun, B. Akuzum, L. Agartan, Y. Gogotsi, E. C. Kumbur, *J. Electrochem. Soc.* **2021**, *168*, 090518.
- [43] T. S. Mathis, K. Maleski, A. Goad, A. Sarycheva, M. Anayee, A. C. Foucher, K. Hantanasisirakul, C. E. Shuck, E. A. Stach, Y. Gogotsi, *ACS Nano* **2021**, *15*, 6420–6429.
- [44] M. Shekhirev, C. E. Shuck, A. Sarycheva, Y. Gogotsi, *Prog. Mater. Sci.* **2021**, *120*, 100757.
- [45] K. Maleski, C. E. Ren, M.-Q. Zhao, B. Anasori, Y. Gogotsi, *ACS Appl. Mater. Interfaces* **2018**, *10*, 24491–24498.
- [46] A. Bhattacharai, P. C. Ghimire, A. Whitehead, R. Schweiss, G. G. Scherer, N. Wai, H. H. Hng, *Batteries* **2018**, *4*, 48.
- [47] P. A. Boettcher, E. Agar, C. R. Dennison, E. C. Kumbur, *J. Electrochem. Soc.* **2015**, *163*, A5244–A5252.
- [48] E. Agar, C. R. Dennison, K. W. Knehr, E. C. Kumbur, *J. Power Sources* **2013**, *225*, 89–94.

Manuscript received: July 15, 2022

Revised manuscript received: September 28, 2022

Version of record online: October 27, 2022